Journal of Power Sources 253 (2014) 27–34

Contents lists available at ScienceDirect

Journal of Power Sources

journal homepage: www.elsevier.com/locate/jpowsour

Size effect of nickel oxide for lithium ion battery anode

Ming-Yao Cheng*, Yun-Sheng Ye, Tse-Ming Chiu, Chun-Jen Pan, Bing-Joe Hwang*

Department of Chemical Engineering, National Taiwan University of Science and Technology, 43, Sec. 4, Keelung Rd., Taipei 10607, Taiwan, ROC

HIGHLIGHTS

- The originally NiO nanostructured electrode is able to reduce the voltage hysteresis loop.
- The 3-D porous nanostructure of NiO remains stable during charge discharge process.
- The *I*–*V* characteristic indicates the high redox reaction kinetics.
- The anomalous high capacity is contributed by the reversible SEI layer.
- The charge discharge energy efficiency can be much improved.

ARTICLE INFO

Article history:
Received 20 September 2013
Received in revised form
7 December 2013
Accepted 10 December 2013
Available online 18 December 2013

Keywords:
Size effect
Nickel oxide
Anode
Lithium ion battery
Conversion reaction

ABSTRACT

In this study, size effect of NiO particles has been studied as the anode material of lithium ion battery. It is found that NiO nanoparticles synthesized in confined space of ordered mesoporous silica behave anomalous high capacity and higher energy efficiency than sub-micro-sized NiO does. The higher energy efficiency is resulted from the reduction of the hysteresis loop between charge and discharge voltage plateaus, the main drawback of conversion reaction-based metal oxide anode materials. The interesting behavior is proposed to be the reversible formation/dissolution of solid electrolyte interphase (SEI) layers associated with 3-D porous, originally nanostructured NiO electrode that is able to remain stable during charge–discharge process.

1. Introduction

Nowadays the requirements of next generation Lithium ion battery need higher energy density, larger specific capacity, better stability and larger temperature operation window. Regarding the progress of next generation anode materials, several Li storage mechanisms, for example, intercalation (graphite), Li-metal alloying, and conversion reaction (Li + metal oxide → LiO + nano-sized metal), have been reported [1–9]. Nevertheless, the novel materials are able to deliver capacities several times higher than that of conventional graphite. However, different materials lead to different challenges that are awaiting solutions. Transition metal oxides, discovered by Tarascon et al. in 2000 [4], show a specific capacity of 2–3 folds to that of commercially adopted graphite (372 mAh g^{-1}). Nevertheless the conversion reaction shows large hysteresis loop between charge and discharge voltage plateau, indicating its low energy efficiency [10–14]. Some studies employ nanostructured metal substrate as current collectors for better performance, however, the results does not show obvious improvement in the reduction of hysteresis loop [13,15].

Considering the details of conversion reaction at 1st charge process, large-sized metal oxide is able to be reduced to form internally nanostructured metals at a relatively low potential than the subsequently charge steps. During charging step, the low-density Li_2O is formed in the matrix, resulting in dispersion of the nanostructured metals in Li_2O matrix. In the discharge process, the electron transfer needs to go through the Li_2O matrix to access the nanostructured metals. The following solid–solid reaction between Li_2O and nanostructured metals may be kinetically limited, resulting in large hysteresis of voltage plateau. In the discharged state, the nanostructured metals are fully oxidized to form nanostructured metal oxide. In a complete charge–discharge cycle, bulk metal oxides transform to nanostructured ones, which can be referred as the electrochemical pulverization process.

In this work, it is intended to have discrete nanoparticles for investigating the difference between internally nanostructured

* Corresponding authors. Tel.: +886 2 27376624.
E-mail addresses: mycheng@mail.ntust.edu.tw, d8906107@mail.ntust.edu.tw (M.-Y. Cheng), bjh@mail.ntust.edu.tw (B.-J. Hwang).

0378-7753/$ – see front matter © 2013 Elsevier B.V. All rights reserved.
http://dx.doi.org/10.1016/j.jpowsour.2013.12.037

electrode (after 1st charge process of large-sized particles) and originally nanostructured electrode. It is expected the originally nanostructured electrode would not undergo electrochemical pulverization since their size scale is close to micro-sized one after 1st discharge and charge process (internally nanostructured metal oxide). The resulting stable electrode micro-/nano-structure for the originally nanostructured electrode may have significant effect to its hysteresis loop.

2. Experimental

To examine the difference, NiO is employed for illustration. Sub-micro-sized and nano-sized NiO particles are prepared to develop the internally nanostructured electrode and original nano-structured one, respectively. The discrete nano-sized NiO particles (referred as Nano-NiO) are prepared with confined synthesis developed in our previous work [16]. The process includes preparation of ordered mesoporous silica host, inclusion of Nano-NiO, and silica host removal, and is described in the following paragraphs.

SBA-15 is selected as the ordered mesoporous silica host, and the standard preparation conditions follow Zhao's work [17]. All chemicals were purchased from Acros (except P-123 from Sigma–Aldrich) and used as-received. For a standard process, 8.5 g of tetraethylorthosilicate (TEOS, 98%) 30 mL de-ionized H_2O were well mixed with 120 mL of 2 N HCl aqueous solution. The step was lasted for 20 h at 308 K. Later, the solution was sealed and statically aged at 373 K for 24 h. The resulting white precipitate was rinsed with de-ionized water and ethanol, and subsequently calcined at 823 K for 3 h. The obtained white powders are the said SBA-15.

For the synthesis of Nano-sized NiO in the pore channels of SBA-15, a modified hydrophobic encapsulation route was used [16]. The precursor solution was prepared with nickel nitrate hexahydrate (99 wt%, 0.035 mol) and citric acid (0.0175 mol) in de-ionized water (20 g). 1 g of SBA-15 was added to the precursor solution with continuous stirring and ultrasonic treatment to ensure complete impregnation of the precursor solution into the pore channels. The mixture was stirred and slowly heated at 60 °C for gradual inclusion of precursor until complete removal of bulk water. The dried powders were heated at a ramping rate of 5 °C min^{-1}–600 °C with further treatment at 600 °C for 1 h.

To release Nano-NiO from the SBA-15, the prepared materials were treated with 100 mL of 2 M NaOH (>99%, ACROS) solution ($EtOH:H_2O$ = 1:1 in vol%) to dissolve the silicate-based SBA-15. After 2 h-dissolution process, Nano-NiO was collected by vacuum filtration with microporous membrane (PVDF membrane filter, pore size: 0.2 μm, PALL). The solids were filtered, rinsed with de-ionized water for several times and dried in the oven at 80 °C.

For synthesis of sub-micron-sized NiO, 0.03 mol $Ni(NO_3)_2 \cdot 6H_2O$ (ACROS) was dissolved in 50 mL de-ionized water. Meanwhile, 0.12 mol NaOH was dissolved in 50 mL de-ionized water followed by dropping into a $Ni(NO_3)_2$ solution to form green precipitates. The precipitates were filtered and washed with de-ionized water for several times and dried at 80 °C. Finally the precipitates were heated at 600 °C for 1hr as the sub-micron-sized NiO (SubM-NiO).

The materials were characterized by XRD, TEM, BET, and TGA. For XRD patterns, a Rigaku D/Max-RC (Japan) diffractometer was operated at 40 kV and 100 mA with a Cu Kα radiation source. Bright-field TEM image was obtained with JEOL JEM-2010 microscope (Japan) with an accelerating voltage of 200 kV. For characterization of aged materials, the cycled cell was disassembled and the materials were scraped from anode active material layer. The scraped materials were rinsed with DEC solvent several times for removal of $LiPF_6$. Multi-point BET surface area was obtained by nitrogen adsorption technique with a Quantachrome AUTOSORB-1 at 77 K in liquid nitrogen bath. TGA was characterized for the cycled anode material of the aged half cell. The cycled anode material was scraped from the anode of the disassembled aged cell (with half cell charged to 3.0 V). The scraped material was rinsed with DEC (diethyl carbonate) several times to eliminate $LiPF_6$. TGA is performed with a ramping rate of 5 °C min^{-1} to a final temperature of 900 °C under flowing air with a rate of 20 mL min^{-1}.

The electrochemical performance of the materials was evaluated with coin cells using Li foil (FMC) as the anode and the fabricated electrode as the cathode. The anode and cathode were separated by a polypropylene separator saturated with 1 M $LiPF_6$ EC (ethylene carbonate)–DEC (diethyl carbonate) electrolyte solution (Tomiyama, EC:DEC = 1:1 in vol%). The fabricated electrode was prepared with slurry-casting method on the Cu foil. The electrode slurry was composed of active material (SubM-NiO or Nano-NiO), PVDF binder (polyvinylidene difluoride, 99%, ACROS) and carbon black (Super-P, Timcal) with a weight ratio of 6:2:2 in NMP (*N*-methyl-2-pyrrolidone, 99.5%, ACROS). The cast Cu foil was then dried in vacuum oven at 120 °C for 6 h. The dried foil was punched into numerous disks of 13 mm in diameter for the electrochemical testing. The active material was about 1 mg for each half cell. The assembled coin cell is galvanostatically cycled between 3 and 0.01 V at a constant C-rate of 0.2C. At the charge voltage of 3 V, the charge mode shifted to constant voltage until the charge current down to 0.05C. Coin cells were used for cyclic voltammetry (CV) and electrochemical impedance spectroscopy (EIS) as well. CV was performed in a potential window of 0.010–3.500 V with a scanning rate of 5 mV min^{-1} for 10 cycles. EIS was acquired at fully charged state of the half cell (in the state of NiO) during CV. The frequency ranges from 10^6 to 10^{-1} Hz with a DC interrupt of 10 mV. The as-assembled state was characterized as well.

3. Results and discussion

Firstly the XRD patterns for Nano-NiO and SubM-NiO are shown in Fig. 1. It is found that the peak broadening characteristic of fcc NiO (JCPDS - ICDD: 38-0715) is shown for Nano-NiO, indicating the nano-sized feature remaining before and after releasing process. For SubM-NiO, the same crystalline structure as Nano-NiO is shown except sharp peak feature in the XRD pattern. The Scherrer equation is adopted for calculation of the averaged grain size with FWHM (full width at half maximum) of the (2 0 0) peak. The averaged grain size for SBA-15-confined Nano-NiO is as small as

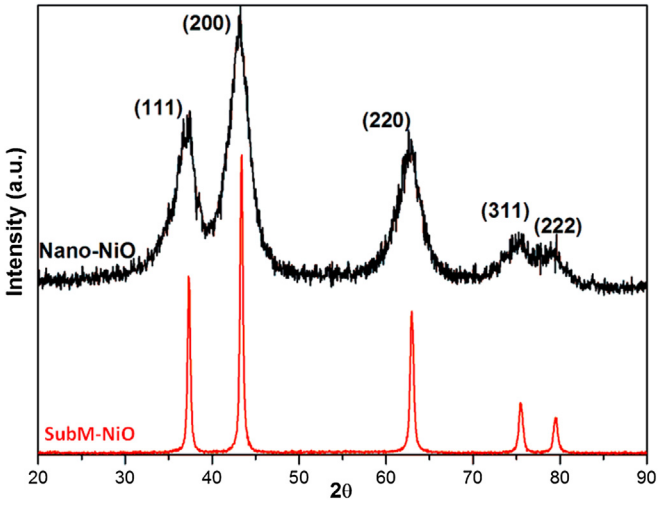

Fig. 1. XRD patterns of Nano-NiO and SubM-NiO.

3.1 nm, which is almost the same as Nano-NiO. For SubM-NiO, the averaged size is about 21.2 nm, which is much higher than that of Nano-NiO. The data coincide with the corresponding specific surface area. The BET surface area for Nano-NiO is 231.60 $m^2 g^{-1}$, which is almost 7-fold the value to that of SubM-NiO (30.05 $m^2 g^{-1}$). Both the smaller grain size and larger BET surface area implies the electrode prepared with Nano-NiO may exhibit much larger exposed surface area to electrolyte than that with SubM-NiO.

TEM of the synthesized materials are then discussed for better understanding the associated morphology. In Fig. 2a and b, the morphologies of ordered mesoporous SBA-15 host are shown. It is observed that uniform 2-D hexagonal arrangement of the pore channels provides a good confined space for synthesis of nanomaterials. From Fig. 2b, the 2-D image of SBA-15 observed from the pore channel direction is shown. Clear, the pore size is around 7.3 nm. From Fig. 2a and b, it is confirmed the success for preparation of ordered mesoporous SBA-15, which is identical to the literature [16–18]. In fact the pore size can be tailored with fine tuning the preparation conditions [18]. The material of Nano-NiO in SBA-15 is examined with TEM as well and shown in Fig. 2c. In the image there are tremendous small nanoparticles inside the pore channels of SBA-15, indicating the confined synthesis of Nano-NiO, which is similar to our previous work [16].

After removal of SBA-15, the obtained Nano-NiO behaves as secondary particles with the size around 50–60 nm that are composed of tremendous small nanoparticles with size ranging from 2 to 4 nm (Fig. 3a). Clearly, no SBA-15 is observed. However about 3 wt% residual SiO_2 is still presented in EDS analysis. Further investigating the small nanoparticles observed in Fig. 3a, the HRTEM image of the small nanoparticles indicates (2 0 0) lattice image of NiO (Fig. 3b). For SubM-NiO, the particle size is around 20–30 nm (Fig. 3c), which is identical to XRD and BET analysis.

To study the electrochemical characteristics of originally nanostructured electrode and internally nanostructured one, the both electrodes associated with Nano-NiO and SubM-NiO as active materials are assembled as coin cells, respectively. Firstly, the constant current charge–discharge cycle with a rate of 0.2C is adopted between 3 and 0.001 V. For charge step, an additional constant voltage charge at 3 V is applied, which the cutoff current is 0.05C. Fig. 4a shows the 1st cycle capacity–voltage curves of the cells assembled with both Nano-NiO and SubM-NiO electrodes, respectively. The discharge plateau of Nano-NiO cell starts from ~1.0 V, which is much higher than SubM-NiO cell (starts from 0.5 V). The difference in 1st plateau implies better reaction kinetics during reduction of Nano-NiO, which may be probably related to the ease in access of Li ions to NiO. For Nano-NiO, the porous secondary particles provide good 3-D channels to access the NiO located inside their core. However the reduction of SubM-NiO by Li ions may start from the surface of sub-micron NiO. Furthermore, the deposited Li_2O during the reduction process may coat on the surface of the subsequent NiO when the outmost NiO has been reduced to Ni. For the case of Nano-NiO, the porous nature of the secondary particles provides some space for accommodation of the deposited Li_2O. Therefore the deposited Li_2O may not hinder the following reduction process of NiO, since the porous structure of Nano-NiO is proposed to provide 3-D channels for Li ions access.

The profile goes down steeply when the voltage is lower than 0.5 V; it is proposed to be the contribution of the solely SEI layers on

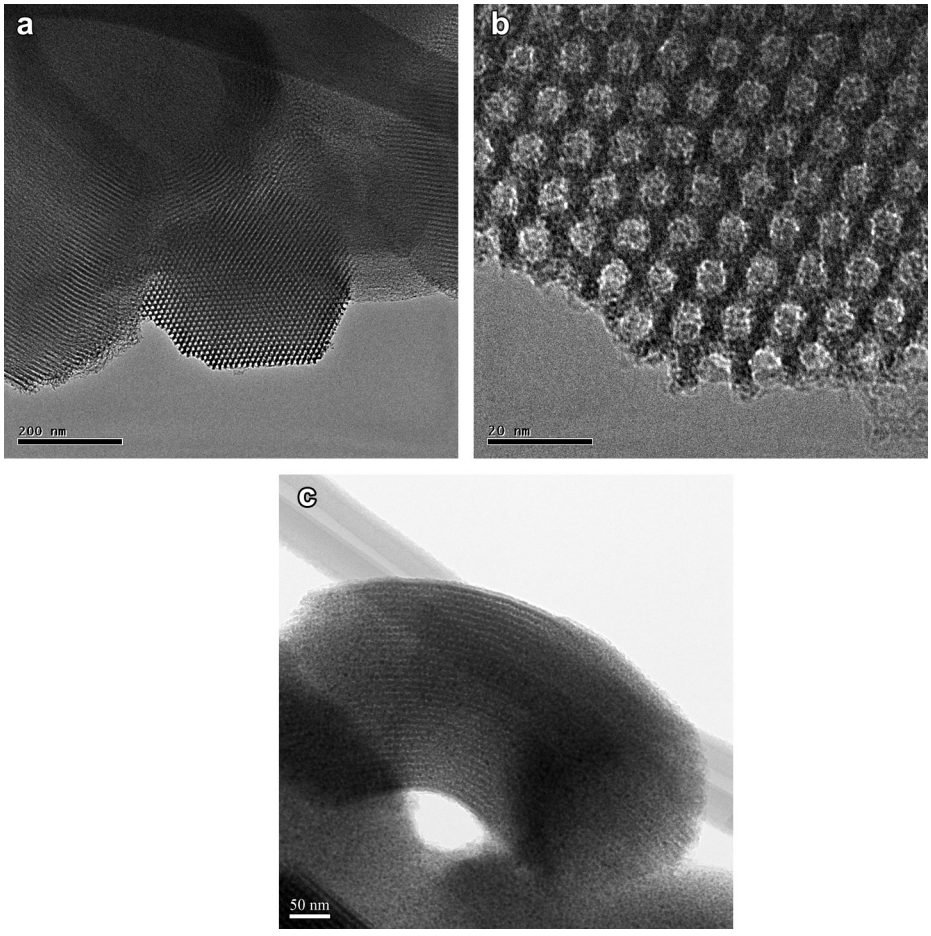

Fig. 2. TEM images of (a) ordered mesoporous SBA-15 (scale bar: 200 nm), (b) ordered mesoporous SBA-15 (scale bar: 20 nm), (c) SBA-15-confined Nano-NiO (scale bar: 50 nm).

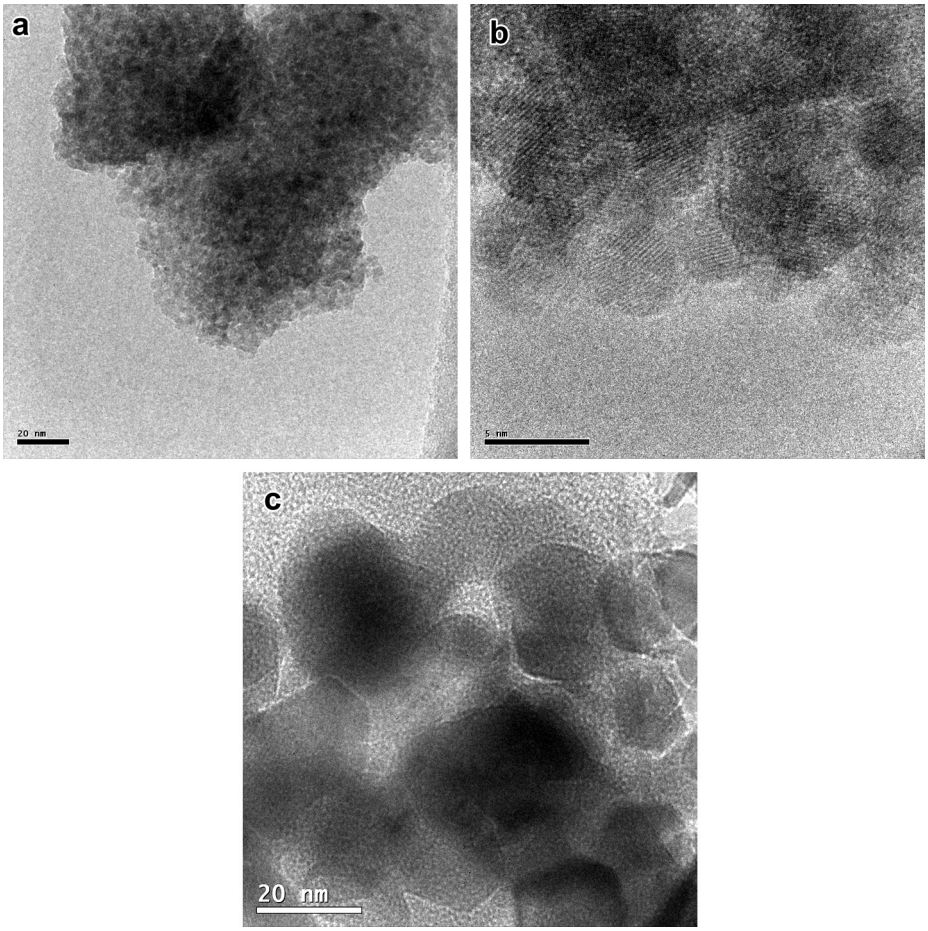

Fig. 3. TEM images of (a) Nano-NiO (scale bar: 20 nm), (b) Nano-NiO (scale bar: 5 nm), and (c) SubM-NiO (scale bar: 20 nm).

the electrode surface [19–23]. The behavior is similar for both SubM-NiO and Nano-NiO cells. The discharge capacity of Nano-NiO cell is around 1500 mAh g^{-1}, much higher than that of SubM-NiO (~900 mAh g^{-1}). The anomalously high capacity of Nano-NiO half cell is proposed to be the contribution of the surfaced SEI layer, which is possibly due to the much higher surface area of Nano-NiO, and can be indirectly supported by the larger plateau slope of Nano-NiO. The result also implies more SEI formed at the potential window of 1–0.5 V for Nano-NiO cell [19–23].

In the charge step, the plateau starts from 1.2 V to 2.1 V for Nano-NiO and SubM-NiO, respectively. Again, the capacity below the plateau voltage results from the reversible dissolution of partial SEI layer [19–23]. The revisable formation/dissolution of partial SEI layer is investigated in literature. As observed in Fig. 4a, the anomalous capacity for Nano-NiO half cell is much higher than that of theoretical NiO (717 mAh g^{-1}) at a current rate of 0.2C. Similar behavior is shown with higher current rate (1C) in Fig. 5a (detail discussion later). In the work of Tarascon et al. [19], it was found as well that the anomalous high capacity of CoO can be observed for the higher testing temperature, and the behavior is reversible with the change of testing temperature. It was suggested that the revisable formation/dissolution of SEI layer is due to the one electron-transferred polymerization of EC by ring opening. On the other hand, firm evidence was provided by Bijani et al. using XAS for understanding the conversion reaction of Cu_2O as anode [23]. They found the valence state of Cu is not fully reduced to metallic state, but the capacity is beyond what Cu^{1+} to Cu^0 can provide, indicating occurrence of another reversible electrochemical process during charge/discharge, which the reversible formation/dissolution of SEI layer is mostly possible.

Further, the large difference in plateau voltage between Nano-NiO and SubM-NiO should be due to the contribution of electronic resistance of Li_2O. Better oxidation reaction kinetics of Nano-NiO cell is supposed to better connectivity of nanostructured Ni since some Li_2O should be deposited in the space of the 3-D porous channels, and therefore the nanostructure of the reduced Ni should be less impacted. The better connectivity of Ni metallic nanostructure leads to easier electronic pathway during oxidation of Ni by Li_2O. Further the 3-D porous structure may also contribute the Li ion transport, and therefore results in less polarization. However, Nano-NiO cell shows the other voltage plateau ranging between 2.15 and 2.30 V, close to SubM-NiO (2.10–2.25 V), indicating part of reduced Ni under similar environment as that of SubM-NiO. The 1st-cycle columbic efficiency of Nano-NiO and SubM-NiO is 70.1% (1053 mAh g^{-1}/1502 mAh g^{-1}) and 72.9% (643 mAh g^{-1}/882 mAh g^{-1}), respectively, which is similar to literature.

Fig. 4b shows 2nd-cycle capacity–voltage curves of the both cells. The columbic efficiencies of the both cells are higher than 95%. Similarly, the better electrochemical reaction kinetic and two voltage plateaus during charge step are observed for Nano-NiO.

Based on 2nd-cycle data shown in Fig. 4b, the accumulated energy to voltage profile and the associated charge–discharge energy efficiency are shown in Fig. 4c. From the area of the accumulated energy–voltage profile (only charge step is shown) of the both SubM-NiO and Nano-NiO, it is clear that Nano-NiO is able to deliver more energy than SubM-NiO. Furthermore, the energy

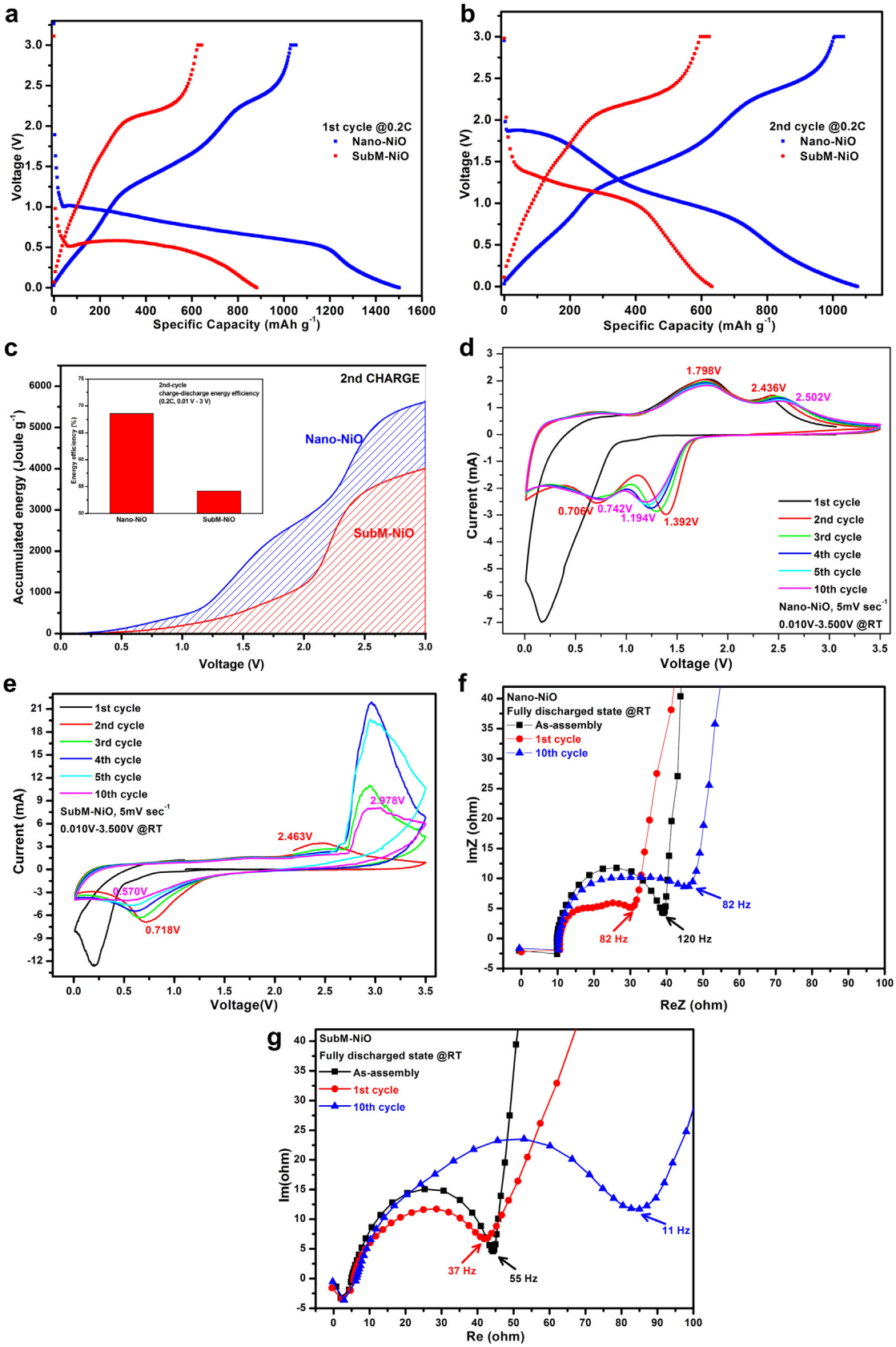

Fig. 4. (a) 1st-cycle *I*–*V* curve, (b) 2nd-cycle *I*–*V* curve, and (c) accumulated energy and (inset) charge–discharge energy efficiency of both Nano-NiO and SubM-NiO (current rate: 0.2C, potential window: 3–0.01 V); CV (d, e) and EIS (f, g) results of Nano-NiO and SubM-NiO.

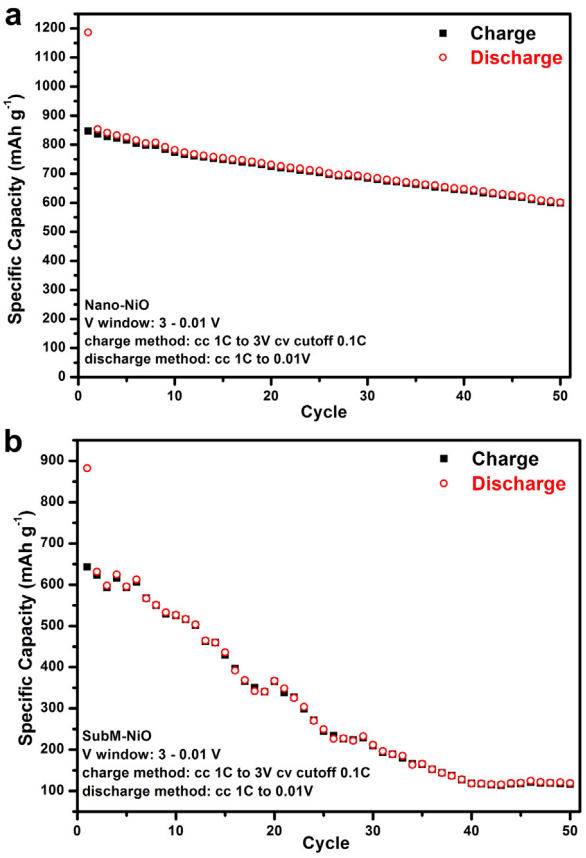

Fig. 5. Charge–discharge life cycle performance of both (a) Nano-NiO and (b) SubM-NiO; (current rate: 1C, potential window: 3–0.01 V).

efficiency of the both half cells can be evaluated with the accumulated charge energy divided by the accumulated discharge energy. As shown in the inset of Fig. 4c, the charge–discharge energy efficiency of SubM-NiO and Nano-NiO under a current rate of 0.2C is 54.2% and 68.6%, respectively, indicating much higher energy efficiency of the originally nanostructured electrode. As discussed in the previous paragraphs, Nano-NiO always shows better redox reaction kinetics over SubM-NiO during both discharge and charge steps. It is believed the better energy efficiency of Nano-NiO is associated with the beneficial 3-D porous nanostructure that can remain stable during charge–discharge process.

Fig. 4d and e discloses the cyclic voltammetry results of the both Nano-NiO and SubM-NiO half cell, respectively. Clearly there are two redox pairs for Nano-NiO, where SubM-NiO exhibits one redox pair only. It is noted that similar behavior is observed in literature [24,25], but neither related investigation nor explanation was shown. The redox peaks of Nano-NiO are stable with further charge–discharge cycling, and only slight shifting for second oxidation peak (2.436–2.502 V from 2nd cycle to 10th cycle) and the both reduction peaks (1.392 and 0.706 V to 1.194 and 0.742 V, respectively, from 2nd cycle to 10th cycle). On the other hand, SubM-NiO shows obvious shift for the both oxidation and reduction peaks (2.463–2.978 V and 0.718–0.570 V, respectively) with serious reduction of the peak magnitude, indicating very poor electrochemical kinetics with fast degradation. Similarly electrochemical impedance spectroscopy (EIS) of the both half cells is characterized at various cycles. For Nano-NiO half cell, the associated impedance shown in Fig. 4f did not show obvious change during CV. The real part of impedance even reduced after 1st cycle (~40–~35 Ω), and increase to 50–55 Ω after 10th cycle. For SubM-NiO, the real part of impedance at initial and after 1st cycle is almost identical to be ~50 Ω, while the capacitative part is slightly reduced (Fig. 4g). After 10th cycle, the real part of impedance is about double of that of the as-assembled one (~100 Ω), indicating serious decay to the as-assembled state. Furthermore, it is also about double of the Nano-NiO after 10th cycle. From CV and EIS results, it is suggested the excellent stability of Nano-NiO while SubM-NiO may degrade in a limited operation time.

Fig. 5 shows the charge–discharge cycle performance at a current rate of 1C of both SubM-NiO and Nano-NiO half cells. Clearly Nano-NiO is able to deliver a charge capacity of 847 mAh g^{-1} at 1st cycle, which is obviously higher than that of SubM-NiO (643 mAh g^{-1}). As the above discussion, the anomalous high capacity of Nano-NiO to the theoretical one (717 mAh g^{-1}) and SubM-NiO as well is proposed to the contribution of reversible formation/dissolution of partial SEI layer [19–23], which is not shown in the micro-sized particles [4], as well as the result of SubM-NiO. The substantial contribution of reversible formation/dissolution of SEI layer to the capacity of Nano-NiO may result from the stable nanostructure during charge–discharge process and much higher BET surface area of Nano-NiO (7 times to that of SubM-NiO). The stable nanostructure during charge–discharge process leads to electrochemically active SEI layer under proper environmental temperature during electrochemical characterization since a stable electron transfer pathway can be remained. On the other hand, higher surface area might possibly provide more active sites for redox reaction of SEI layer. After 50 cycles, Nano-NiO shows 30% capacity loss, whether the capacity of SubM-NiO drops quickly and only 100 mAh g^{-1} left after 40 cycles. The charge–discharge cycle performance indicates the nanostructure of Nano-NiO is much stable to that of SubM-NiO, even the current rate as high as 1C. The cycle performance is highly correlated with CV and EIS results shown from Fig. 4d–g.

To understand the micro/nano-structure after cycling, the cycled electrodes are characterized with TEM. In Fig. 6a, the aged Nano-NiO electrode shows porous nanostructure filled with amorphous materials, which is suggested to be the SEI layer. By the way, the NiO nanoparticles exhibit good interconnection each other with the size remaining 2–3 nm. For SubM-NiO electrode, the structure shown in Fig. 6b is similar to that of Nano-NiO does. However, the size of NiO varies from several to several 10 nm (lower magnification image shown in Fig. 6c), which might be associated with the poor performance of SubM-NiO.

Further, the amount of SEI layer is studied using TGA for better understanding of electrode stability as well. The material is collected from the cycled electrode and rinsed with DEC to remove possible $LiPF_6$ inside. After drying at ambient temperature, the powders are subjected to TGA with a ramping rate of 5 °C min^{-1} until 900 °C in flowing air of 20 mL min^{-1}. Fig. 7 is the TGA results for the both aged Nano-NiO and SubM-NiO electrode materials. It should be noted in advance that the dramatic weight loss before 300 °C and 450 °C should be contributed from PVDF and carbon black, respectively, which the associated decomposition temperatures could be reduced by the presence of catalytic Ni/NiO during heating. The contribution from SEI layer is not as obvious as PVDF and carbon black since the diverse composition with various species. By simple calculation with the formula [W_{NiO}/($W_{SEI} + W_{PVDF} + W_{carbon} + W_{NiO}$) = residual weight percentage by TGA] and the recipe of electrode composition, the weight percent of SEI can be calculated. In the formula, W_{SEI}, W_{PVDF}, W_{carbon}, and W_{NiO} is the weight percentage of SEI layer, PVDF, carbon black, and NiO, respectively. It is found that W_{SEI} is 10.60 wt% and 28.12 wt% for the both Nano-NiO and SubM-NiO electrodes, respectively. From the result, it is suggested that the new surface of the active material of SubM-NiO electrode continuously exposes to electrolyte in the

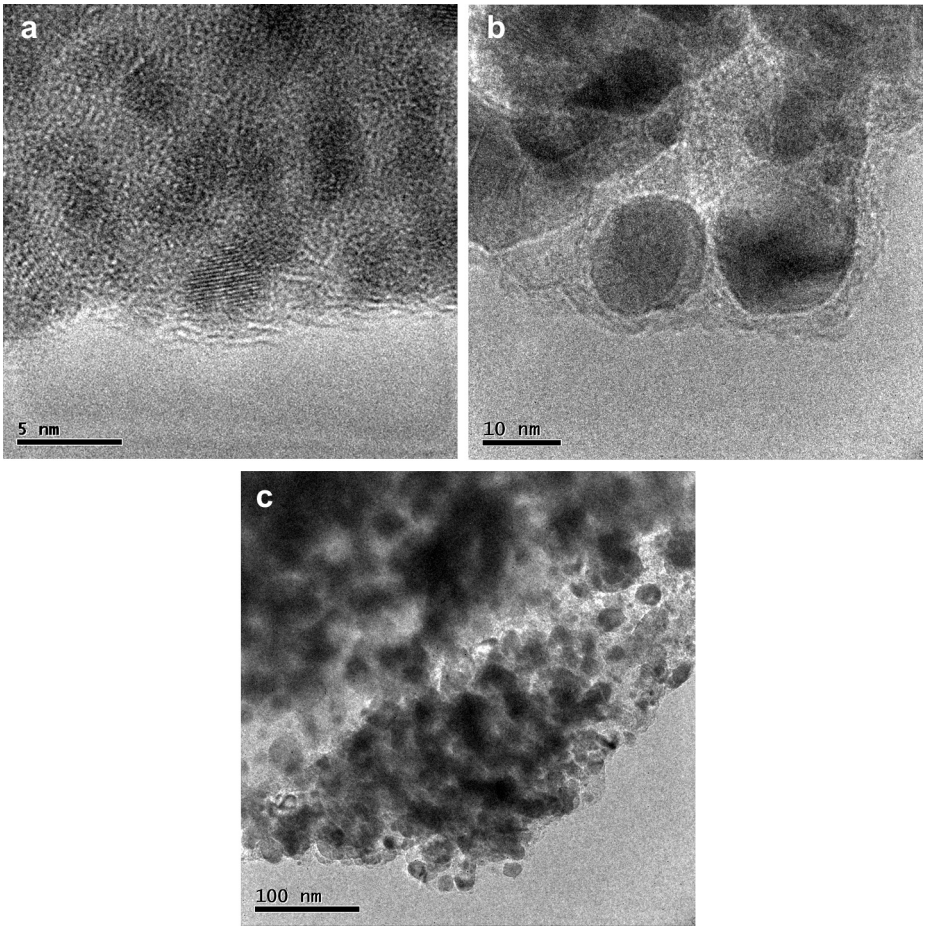

Fig. 6. TEM images of cycled NiO (a) Nano-NiO (scale bar: 5 nm), (b) SubM-NiO (scale bar: 10 nm), and (c) SubM-NiO (scale bar: 100 nm).

reduction step during cycling. Subsequently the new SEI layer forms by the catalytic reaction of new active material surface (NiO/Ni), which leads to continuous isolation of active material by the produced SEI. It is the main reason for poor performance of SubM-NiO electrode.

4. Conclusion

It is found that the originally nanostructured electrode by the discrete NiO nanoparticles shows curious electrochemical properties compared to internally nanostructured one by sub-micron/micron NiO particles. The two voltage plateaus of Nano-NiO with much better redox reaction kinetics, and the contribution of porous 3-D nanostructure, indicate its higher energy efficiency to SubM-NiO. Further the stable nanostructure and high surface area of Nano-NiO improve the cycle life and the reversible redox reaction of SEI layers, resulting in higher reversible capacity. It can be concluded that the originally nanostructured electrode by discrete NiO nanoparticles is able to reduce the charge–discharge hysteresis loop, the typical drawback of conversion reaction-type Li-ion battery anode materials, and therefore leads to better energy efficiency, higher reversible capacity, and stable cycle performance.

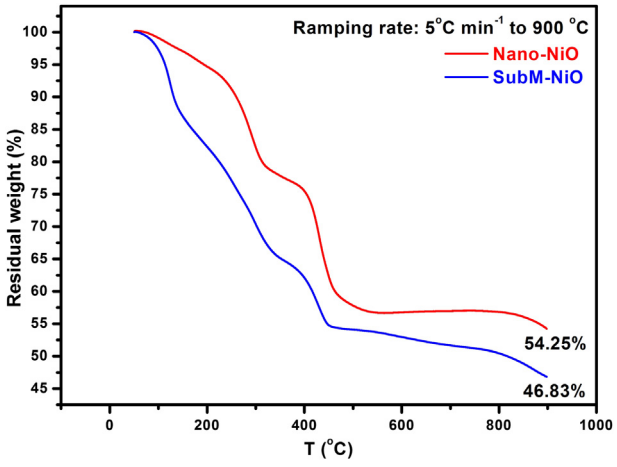

Fig. 7. TGA of cycled Nano-NiO and SubM-NiO.

Acknowledgments

The financial supports from the National Science Council (NSC) (101-3113-E-011-002, 101-2923-E-011-001-MY3), the Ministry of Economic Affairs (MOEA) (101-EC-17-A-08-S1-183), and the Top University Projects of Ministry of Education (MOE) (100H451401), as well as the facilities supports from the National Taiwan University of Science and Technology (NTUST) are acknowledged.

References

[1] D. Aurbach, B. Markovsky, S.F. Amalraj, H. Gottlieb, Y. Gofer, S.K. Martha, J. Electrochem. Soc. 157 (2010) A423.
[2] J.B. Goodenough, Y. Kim, Chem. Mater. 22 (2009) 587.
[3] M.Y. Cheng, C.L. Hwang, C.J. Pan, J.H. Cheng, Y.S. Ye, J.F. Rick, B.J. Hwang, J. Mater. Chem. 21 (2011) 10705.

[4] P. Poizot, S. Laruelle, S. Grugeon, L. Dupont, J.-M. Tarascon, Nature 407 (2000) 496.
[5] M.Y. Cheng, B.J. Hwang, J. Power Sources 195 (2010) 4977.
[6] Y.-N. Nuli, S.-L. Zhao, Q.-Z. Qin, J. Power Sources 114 (2003) 113.
[7] Z. Yang, D. Choi, S. Kerisit, K.M. Rosso, D. Wang, J. Zhang, G. Graff, J. Liu, J. Power Sources 192 (2009) 588.
[8] J. Kim, J. Cho, Electrochem. Solid State Lett. 10 (2007) A81.
[9] H. Zhou, S. Zhu, M. Hibino, I. Honma, M. Ichihara, Adv. Mater. 15 (2003) 2107.
[10] V. Etacheri, R. Marom, R. Elazari, G. Salitra, D. Aurbach, Energy Environ. Sci. 4 (2011) 3243.
[11] M.G. Kim, J. Cho, Adv. Funct. Mater. 19 (2009) 1497.
[12] Y. Yu, C.-H. Chen, Y. Shi, Adv. Mater. 19 (2007) 993.
[13] P.L. Taberna, S. Mitra, P. Poizot, P. Simon, J.M. Tarascon, Nat. Mater. 7 (2006) 567.
[14] J.-M. Tarascon, S. Grugeon, S. Laruelle, D. Larcher, P. Poizot, in: G.A. Nazri, G.Pistoia (Eds.), Lithium Batteries—Science and Technology, Kluwer Academic Publishers, Boston, 2003 (Chapter 7).
[15] F. Gillot, S. Boyanov, L. Dupont, M.L. Doublet, M. Morcrette, L. Monconduit, J.M. Tarascon, Chem. Mater. 17 (2005) 6327.
[16] M.Y. Cheng, C.J. Pan, B.J. Hwang, J. Mater. Chem. 19 (2009) 5193.
[17] D. Zhao, Q. Huo, J. Feng, B.F. Chmelka, G.D. Stucky, J. Am. Chem. Soc. 120 (1998) 6024.
[18] Y. Xia, Z. Yang, R. Mokaya, Chem. Mater. 18 (2006) 140.
[19] S. Grugeon, S. Laruelle, L. Dupont, J.M. Tarascon, Solid State Sci. 5 (2003) 895.
[20] R. Dedryvere, S. Laruelle, S. Grugeon, P. Poizot, D. Gonbeau, J.M. Tarascon, Chem. Mater. 16 (2004) 1056.
[21] S. Grugeon, S. Laruelle, R. Herrera-Urbina, L. Dupont, P. Poizot, J.-M. Trarscon, J. Electrochem. Soc. 148 (2001) A285.
[22] C.H. Chen, B.J. Hwang, J.S. Do, J.H. Weng, M. Venkateswarlu, M.Y. Cheng, R. Santhanam, K. Ragavendran, J.F. Lee, J.M. Chen, D.G. Liu, Electrochem. Commun. 12 (2010) 496.
[23] S. Bijani, M. Gabás, G. Subías, J. García, L. Sánchez, J. Morales, L. Martínez, J.R. Ramos-Barrado, J. Mater. Chem. 21 (2011) 5368.
[24] X.-J. Zhu, J. Hu, H.-L. Dai, L. Ding, L. Jiang, Electrochim. Acta 64 (2012) 23.
[25] C. Xu, J. Sun, L. Gao, J. Power Sources 196 (2011) 5138.